Multimode non-Hermitian framework for third harmonic generation in nonlinear photonic systems comprising two-dimensional materials

Thomas Christopoulos [1,2,*] Emmanouil E. Kriezis [2] and Odysseas Tsilipakos [3,1,†]

[1]*Institute of Electronic Structure and Laser, Foundation for Research and Technology Hellas (FORTH), Heraklion 70013, Crete, Greece*
[2]*School of Electrical and Computer Engineering, Aristotle University of Thessaloniki (AUTH), GR-54124 Thessaloniki, Greece*
[3]*Theoretical and Physical Chemistry Institute, National Hellenic Research Foundation, GR-11635 Athens, Greece*

Resonant structures in modern nanophotonics are non-Hermitian (leaky and lossy), and support quasinormal modes. Moreover, contemporary cavities frequently include two-dimensional (2D) materials to exploit and resonantly enhance their nonlinear properties or provide tunability. Such materials add further modeling complexity due to their infinitesimally thin nature and strong dispersion. Here, a formalism for efficiently analyzing third harmonic generation (THG) in nanoparticles and metasurfaces incorporating 2D materials is proposed. It is based on numerically calculating the quasinormal modes in the nanostructure, it is general, and does not make any prior assumptions regarding the number of resonances involved in the conversion process, in contrast to conventional coupled-mode theory approaches in the literature. The capabilities of the framework are showcased via two selected examples: a single scatterer and a periodic metasurface incorporating graphene for its high third-order nonlinearity. In both cases, excellent agreement with full-wave nonlinear simulations is obtained. The proposed framework may constitute an invaluable tool for gaining physical insight into the frequency generation process in nano-optic structures and providing guidelines for achieving drastically enhanced THG efficiency.

I. INTRODUCTION

Nonlinear light-matter interactions are an indispensable ingredient in contemporary optical systems since they allow for advanced functionalities [1,2], well beyond the reach of linear phenomena. Harmonic generation, parametric amplification, frequency mixing, multiphoton and saturable absorption, self- and cross-phase modulation are only some of the most notable nonlinear effects [3]. Nonlinear optics first flourished in bulk crystals and optical fibers where long interaction lengths are available. The recent shift towards compact nanophotonic systems and ultrathin metasurfaces limits the interaction length or volume between the optical field and the nonlinear material, necessitating different physical approaches in order to achieve strong nonlinear effects. More specifically, these include (i) the exploitation of resonant structures with high quality factors to confine energy temporally [4] and small mode volume to confine energy spatially producing enhanced local fields [5], and (ii) the utilization of highly nonlinear materials, be it bulk (nonlinear polymers, chalcogenide glasses, etc.) or, more recently, the emerging category of sheet, two-dimensional (2D) materials [6,7]. Sheet materials [graphene, transition metal dichalcogenides (TMDs), black phosphorus, MXenes, etc.] have illustrated great potential for photonic and optoelectronic applications [8–10]. However, they also introduce complexity when incorporated in a nanophotonic system, both in terms of its practical realization, as well as its efficient

analysis and design, e.g., their atomic thickness and strong dispersion needs to be handled carefully.

Here, we focus on how the two-dimensional nature as well as the lossy and dispersive properties of 2D materials should be handled rigorously in the context of modal analysis tools for open (leaky) resonant third-order nonlinear systems. Note that practically all modern nanophotonic systems, including dielectric and plasmonic particles, periodic metasurfaces, photonic crystal membranes, and compact guided-wave resonators, exhibit significant radiation leakage. Such contemporary systems can be efficiently studied using modal techniques, a research direction which has gathered significant interest recently [11–15]. Initially, researchers focused on developing a *linear* framework capable of handling non-Hermitian resonant structures (leaky and lossy) comprised of *bulk* materials. The supported quasinormal eigenmodes (QNMs) diverge in space away from the resonator and their correct normalization became the subject of numerous studies [5,16–19]. Building upon this normalization, a number of techniques to reconstruct the full spectrum of a system using the supported QNMs were presented [20–26]. Other important aspects have been discussed as well, such as completeness and orthogonality of the expansion [12,14,15], and the importance of including static modes on the expansion [27,28]. Furthermore, related classical theoretical tools of Hermitian analysis, such as perturbation theory [29–32] and temporal coupled-mode theory (CMT) [32–35], were modified to become applicable to QNMs and non-Hermitian systems.

Despite the progress concerning linear systems, very limited focus has been directed to the wider class of nonlinear non-Hermitian systems [32,36]. In this work, we contribute

*cthomasa@iesl.forth.gr
†otsilipakos@eie.gr

towards this important direction by developing a QNM-based, multimode third-order nonlinear framework which allows to include 2D photonic materials with loss and dispersion within the resonant structure. It builds on Ref. [36], which discusses bulk materials and second-order nonlinearity. Our contribution is twofold: (i) it introduces 2D materials in a linear QNM framework, naturally incorporating their unique infinitesimally thin nature and dispersive properties, and (ii) it contributes into the exploitation of their third-order nonlinear properties for efficient frequency generation, under the same QNM perspective. The developed framework can aid in efficiently analyzing and designing general resonant systems comprising bulk *and* sheet materials, as well as gaining valuable physical insight into the resonances mediating the conversion process and developing design directives for obtaining efficient performance.

II. THIRD HARMONIC GENERATION FRAMEWORK FOR PHOTONIC SCATTERERS INCLUDING 2D MATERIALS

The proposed nonlinear framework is based on the ability to calculate the response of a resonant system upon a prescribed excitation by using a finite set of QNMs [11,15]. The first step towards this goal is to correctly calculate and normalize the supported QNMs, a nontrivial task in non-Hermitian systems [5,16–19] due to the fact that the mode profile outside a resonant cavity diverges [4]. To computationally calculate and normalize the supported QNMs, we build upon Refs. [21,37], extending the methodology in order to tackle contemporary photonic structures including 2D and bulk materials with lossy and dispersive electomagnetic properties.

For brevity, below we present the derivation concerning the 2D material inclusions; the complete case can be found in Appendix A. Henceforth, a 2D material with a Drude-type complex surface conductivity (measured in S) of the form $\bar{\bar{\sigma}}_s(\omega) = -j\bar{\bar{\sigma}}_0/(\omega - j\gamma)$ is assumed. It is convenient to express the source-free curl Maxwell's equations using the compact notation $\hat{\mathcal{L}}\tilde{\boldsymbol{\Psi}}_m = \tilde{\omega}_m \tilde{\boldsymbol{\Psi}}_m$, where $\tilde{\boldsymbol{\Psi}}_m = [\tilde{\mathbf{H}}_m \ \tilde{\mathbf{E}}_m \ \tilde{\mathbf{J}}_m]^T$ is a supervector containing the involved electromagnetic fields, m is a general index of the QNM order, $\hat{\mathcal{L}}$ is a curl operator (in matrix notation)

$$\hat{\mathcal{L}} = \begin{bmatrix} 0 & j\mu^{-1}\boldsymbol{\nabla}\times & 0 \\ -j\varepsilon^{-1}\boldsymbol{\nabla}\times & 0 & -\varepsilon^{-1} \\ 0 & -\bar{\bar{\sigma}}_0\delta_s & j\gamma \end{bmatrix}, \quad (1)$$

$\tilde{\mathbf{J}}_m = -\bar{\bar{\sigma}}_0/(\tilde{\omega}_m - j\gamma)\tilde{\mathbf{E}}_m\delta_s$ is a surface auxiliary field that is used to introduce the dispersive nature of the 2D material, and $\delta_s \equiv \delta_s(\mathbf{r})$ is a surface Dirac function used to capture the presence of the 2D material. Note that $\tilde{\mathbf{J}}_m$ does not correspond to the (surface) current density $\tilde{\mathbf{J}}_s = \bar{\bar{\sigma}}_s\tilde{\mathbf{E}}\delta_s$ of the Maxwell's equations (they differ by a prefactor j). The tilde in the fields denotes modal quantities. Similarly, $\tilde{\omega}_m$ is the respective complex eigenvalue of the mth-order QNM; the imaginary part carries information regarding the linewidth of the mode. The second-rank tensor $\bar{\bar{\sigma}}_0$ is introduced to encapsulate the 2D nature of the involved material in the sense that the field interacts with the sheet material only through its tangential field components. Finally, γ describes damping due to Ohmic loss.

It has been shown that due to the orthonormality of QNMs [21], scattered field of a resonator can be expanded into an infinite sum of the form $\boldsymbol{\Psi}_{\text{sct}}(\omega) = \sum_m a_m(\omega)\tilde{\boldsymbol{\Psi}}_m$, where the expansion coefficients $a_m(\omega)$ are calculated through (see Appendix A)

$$a_m(\omega) = \frac{1}{\tilde{\omega}_m - \omega} \int_V \tilde{\mathbf{J}}_m \cdot \mathbf{E}_{\text{inc}} dV, \quad (2)$$

where $\mathbf{E}_{\text{inc}}$ is the incident field that excites the resonant scatterer at the real frequency ω and must include possible reflections from the background [19]. Equation (2) applies only when a (surface) conductivity term is present; for the more general case of bulk *and* sheet materials, see Appendix A. Although the completeness of the expansion is not strictly ensured for any arbitrary geometry, it is widely accepted that the expansion is complete inside and in the vicinity of the resonant cavity [14,15]. In Eq. (2), all the involved modes are normalized such that

$$\int_V \left(\tilde{\mathbf{E}}_m \cdot \varepsilon \tilde{\mathbf{E}}_m - \tilde{\mathbf{H}}_m \cdot \mu \tilde{\mathbf{H}}_m - \tilde{\mathbf{E}}_m \cdot j \frac{\partial \bar{\bar{\sigma}}_s(\omega)}{\partial \omega}\bigg|_{\omega = \tilde{\omega}_m} \tilde{\mathbf{E}}_m \delta_s \right) dV = 1. \quad (3)$$

Equations (2) and (3) are key ingredients in the description of linear resonant systems incorporating dispersive 2D materials with the QNM framework. The last term on the left-hand side of Eq. (3) is an important and necessary addition, providing the correct normalization of the QNMs when the nanophotonic resonator includes 2D materials; recently, we have revealed a similar contribution in the normalization for Hermitian (or quasi-Hermitian) systems [38]. Omitting this term introduces large errors [38], especially when dispersion is strong [see spectral derivative in Eq. (3) and the Supplemental Material [39], Sec. S1.iii for a comparison]. Note that in order to correctly evaluate Eq. (3) one has to terminate the computational domain with perfectly matched layers (PMLs) and perform the integration inside the artificial domains as well [5]. Alternatively, an appropriate surface term should be added to truncate the infinite space into a finite computational domain [16]. In this case, the applicability is limited to systems with a uniform background material [14].

A similar approach can be followed to describe *nonlinear* effects, as shown in Ref. [36] for the case of bulk materials and second-order nonlinearity. In this work, we allow for the inclusion of 2D materials and focus on third-order nonlinearities and third harmonic generation (THG) in particular. Note that coupled-mode theory frameworks involving a single mode in each of the fundamental and the third harmonic frequencies exist in the literature [40,41]. However, they fail to capture the correct physical picture when more resonances are involved in the conversion process. In sharp contrast, the proposed *multimode* framework allows for interaction between all the supported QNMs without making any prior assumptions regarding which modes mediate the conversion process. We start by writing the scattered fields at the fundamental and third harmonic frequencies as

$$\hat{\mathcal{L}}\boldsymbol{\Psi}_{\text{sct}}^{(\omega)} = \omega\boldsymbol{\Psi}_{\text{sct}}^{(\omega)} + \mathbf{S}_{\text{inc}}^{(\omega)}, \quad (4a)$$

$$\hat{\mathcal{L}}\boldsymbol{\Psi}_{\text{sct}}^{(3\omega)} = 3\omega\boldsymbol{\Psi}_{\text{sct}}^{(3\omega)} + \mathbf{S}_{\text{inc}}^{(3\omega)}, \quad (4b)$$

where $\mathbf{S}_{\text{inc}}^{(\omega)} = [0 \;\; 0 \;\; \bar{\bar{\sigma}}_0 \mathbf{E}_{\text{inc}} \delta_s]^T$ is the direct excitation at ω (e.g., an appropriately polarized plane wave) and $\mathbf{S}_{\text{inc}}^{(3\omega)} = [0 \;\; -j\varepsilon^{-1}\mathbf{J}_{s,\text{NL}}^{(3\omega)}\delta_s \;\; 0]^T$ is the induced nonlinear source at 3ω (no direct external excitation at 3ω takes place). The induced nonlinear surface current at 3ω $\mathbf{J}_{s,\text{NL}}^{(3\omega)} = (\sigma_3/4)(\mathbf{E}_{t,\parallel}^{(\omega)} \cdot \mathbf{E}_{t,\parallel}^{(\omega)})\mathbf{E}_{t,\parallel}^{(\omega)}$, acting as the source at the third harmonic frequency, is determined from the nonlinear interaction between the total tangential electric field components at the fundamental frequency, i.e., the sum of the incident, reflected from the background, and scattered fields ($\mathbf{E}_t^{(\omega)} = \mathbf{E}_{\text{inc}}^{(\omega)} + \mathbf{E}_r^{(\omega)} + \mathbf{E}_{\text{sct}}^{(\omega)} = \mathbf{E}_b^{(\omega)} + \mathbf{E}_{\text{sct}}^{(\omega)}$). The nonlinear surface conductivity σ_3 is the only independent element of the respective, fourth-order nonlinear tensor [38]. By substituting the QNM expansion at the fundamental frequency in Eq. (4a) and following a procedure similar to Ref. [21], we can retrieve Eq. (2) (see also Appendix A). In a completely analogous manner, we substitute the respective expansion at the third harmonic frequency $\mathbf{\Psi}_{\text{sct}}^{(3\omega)} = \sum_m a_m(3\omega)\tilde{\mathbf{\Psi}}_m$ in Eq. (4b) and arrive at

$$a_m(3\omega) = \frac{-j}{\tilde{\omega}_m - 3\omega} \int_V \tilde{\mathbf{E}}_m \cdot \mathbf{J}_{s,\text{NL}}^{(3\omega)} \delta_s \, dV. \tag{5}$$

Equation (5) constitutes the second and most important result of this work. It allows to calculate the expansion coefficients and, thus, the nonlinear response of a resonant system with third-order nonlinear sheet materials. To do so, one first needs to specify the nonlinear current $\mathbf{J}_{s,\text{NL}}^{(3\omega)}$ using the scattered $\mathbf{E}_{\text{sct}}^{(\omega)}$ and the background $\mathbf{E}_b^{(\omega)} = \mathbf{E}_{\text{inc}}^{(\omega)} + \mathbf{E}_r^{(\omega)}$ fields at the fundamental frequency. $\mathbf{E}_{\text{sct}}^{(\omega)}$ is reconstructed from the eigenmodes and their respective amplitudes $a_m(\omega)$ while $\mathbf{E}_b^{(\omega)}$ is calculated either analytically or numerically in the absence of the resonant cavity. We shall highlight that when $\mathbf{E}_b^{(\omega)} \neq \mathbf{E}_{\text{inc}}^{(\omega)}$ (i.e., in the presence of a substrate), the former should replace the latter even when $a_m(\omega)$ are calculated. Then, the scattered field at the third harmonic $\mathbf{E}_{\text{sct}}^{(3\omega)}$ can be reconstructed using the same eigenmodes but weighted with the new amplitudes $a_m(3\omega)$ [Eq. (5)] (now the QNMs in the neighborhood of 3ω are expected to mainly contribute). Note that this strategy cannot take into account neither the power lost from the field at the fundamental frequency nor the back-conversion from the third harmonic to the fundamental frequency. It is termed the *undepleted pump* approximation and is accurate for moderate conversion efficiencies, as discussed below [42].

III. EVALUATION OF NONLINEAR FRAMEWORK IN GRAPHENE-COMPRISING RESONANT SYSTEMS

To highlight the capabilities of the developed nonlinear framework, we analyze two resonant structures comprising graphene, the most prominent representative of the 2D materials family. We choose THz frequencies where graphene supports tightly confined surface plasmons (GSPs) [43]. The two structures under study are depicted in Fig. 1. The first is a single scatterer: a graphene strip lying on a glass substrate [Fig. 1(a)]. The second is a periodic system derived from the first one, i.e., a metasurface made of periodically arranged graphene strips on a metal-backed substrate to operate in reflection [Fig. 1(b)]. Transverse-magnetic (TM) polarized incidence in the xy plane is considered in order to excite
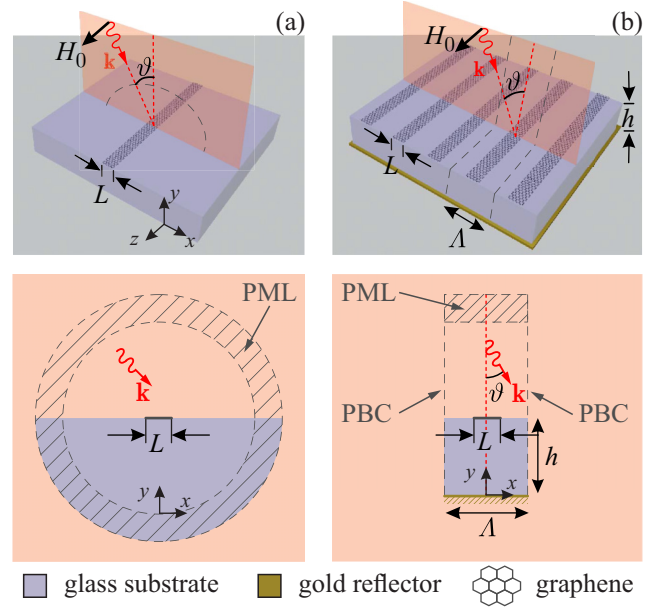

FIG. 1. Schematic illustration of the two graphene-based resonant systems under study. (a) Single scatterer: a graphene strip of length L resides on a glass substrate. (b) Periodic system: a metasurface comprised of graphene strips with pitch Λ on top of a metal-backed substrate to operate in reflection. The metasurface is designed to act as a perfect absorber for a specific QNM. TM-polarized incidence inside the xy-plane is considered ($\mathbf{H} \equiv H_z\hat{\mathbf{z}}$) in order to excite graphene surface plasmons propagating along the x axis. The bottom panels depict the considered two-dimensional computational domains along with the perfectly matched layers (PMLs) used for window truncation. In order to correctly evaluate Eq. (3), one has to perform the integration inside the PMLs as well.

graphene surface plasmons propagating along the x axis. In what follows, the response of both systems around the third harmonic frequency is studied using the developed QNM framework and validated through nonlinear full-wave simulations [42].

A. Graphene-strip single scatterer on a glass substrate

We first consider a single graphene strip of length $L = 5$ μm, lying on a glass substrate with $n = 1.45$ [Fig. 1(a)]. Graphene conductivity in the THz frequency band has a strongly dispersive Drude-type behavior; as is the case with metals below the plasma frequency, this allows for supporting strongly confined plasmons [43]. Here, we adopt the parameters $\gamma = 1/40$ Trad/s, $\sigma_0 = e^2\mu_c/\pi\hbar^2$, and $\mu_c = 0.3$ eV for its linear properties [44] and $\sigma_3 = +j1.2 \times 10^{-18}$ S(m/V)^2 to describe the third-order nonlinear response [45]. Using the commercial finite element method software COMSOL MULTIPHYSICS®, we are able to calculate the QNMs of this leaky and dispersive system, building on the auxiliary-fields approach presented in Refs. [21,37] and appropriately extending it to include sheet materials with Drude dispersion such as graphene. A relatively small set of the eigenmode solutions returned by the solver of COMSOL is depicted in Fig. 2. All QNMs are clearly marked with a red "X" indicator and have a relatively small imaginary part which results in quality factors
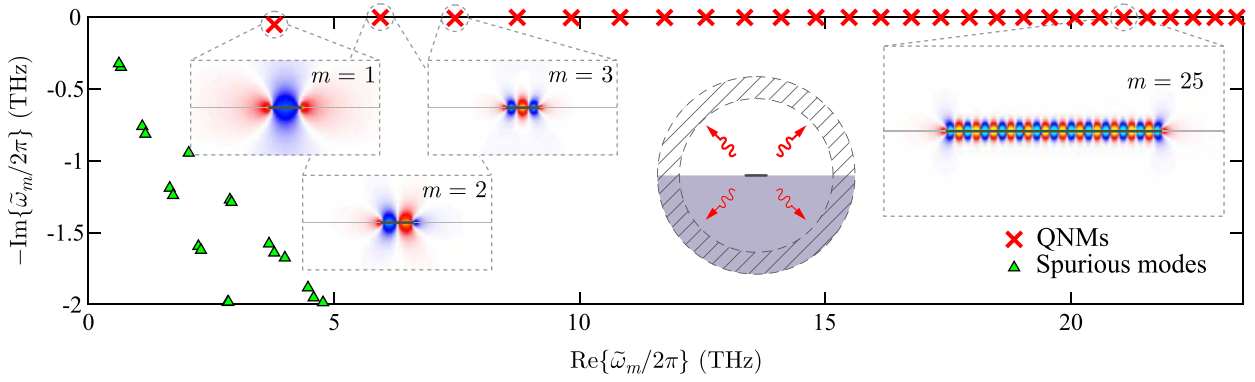
FIG. 2. Spectrum of QNMs and spurious modes for the examined graphene-strip scatterer. Red "X" markers designate the QNMs. They all have small imaginary parts indicating high quality factors. They are unevenly spaced along the real axis due to graphene dispersion. The mode profiles (E_x component) are included as insets for the three lowest-order modes and one higher-order ($m = 25$) mode, lying closest to the third harmonic frequency of the $m = 3$ mode, which will be exploited for the excitation at the fundamental frequency. Green triangle markers highlight a few spurious modes, which are also included in the expansions to obtain better accuracy.

ranging from a few 10's/100's (low-order modes) to a few 1000's (higher-order modes). They correspond to standing waves of GSPs propagating along the x axis and getting reflected at the edges of the finite strip, satisfying a Fabry-Pérot–type resonant condition of the form $2k_\parallel^{\mathrm{GSP}}L + 2\phi_r = n2\pi$, where $\phi_r \approx -3\pi/4$ is the reflection phase at the strip termination [46], which is almost dispersionless as we have numerically verified and differs from the expected $-\pi$ reflection phase of, e.g., plasmons in metals. Note that the integer n does not coincide with the mode index m, which measures the number of half-wavelengths along the graphene strip. The reflection phase ϕ_r and the phase accumulated as the GSP propagates ($k_\parallel^{\mathrm{GSP}}L$) are of opposite signs and the resonance condition of, e.g., the $m = 3$ QNM is fulfilled at a total accumulated phase of 4π, i.e., $n = m - 1$ here. The Fabry-Pérot nature of the modes is also verified by the equidistant spacing when momentarily considering a nondispersive (unphysical case) graphene strip (see the Supplemental Material, Fig. S2 [39]). The field profiles of a few QNMs are included as insets, showing the three lowest-order modes and a higher-order one ($m = 25$). The $m = 25$ mode is the closest to the third harmonic frequency of the $m = 3$ order mode ($\omega_{\mathrm{res},3}/2\pi = 7.46$ THz and $\omega_{\mathrm{res},25}/2\pi = 22.49$ THz), which is chosen to act as the fundamental mode, i.e., to accommodate the excitation at the fundamental frequency. This is justified by the fact that $m = 3$ is the first symmetric (bright) mode with a high quality factor (exceeding 100), thus providing strong resonant enhancement to boost the conversion process. Note that antisymmetric modes cannot be excited with a normally incident plane wave (see Supplemental Material, Sec. S2.i, for a relevant discussion [39]). Despite being of Fabry-Pérot type, the QNMs are unevenly spaced, a direct consequence of the highly dispersive conductivity of graphene and, to a much lesser extent, of the dispersion of the reflection phase ϕ_r experienced by the propagating GSP at the edges of the strip [46] (see Supplemental Material, Sec. S1.i, for the pole structure of the system when material dispersion is momentarily ignored [39]). Thus, we do not find a QNM at exactly $3\omega_{\mathrm{res},3}$ but rather one lying in its vicinity, and the respective mode order is $m = 25$ instead of $m = 9$.

Spurious modes are also returned by the COMSOL eigensolver and are marked with green triangles in Fig. 2 (see also the Supplemental Material, Fig. S1, for a more expanded spectrum [39]). These modes, mainly located either inside the PML (PML modes) or spanning the entire computational domain, should be included in the calculations to ensure the best possible accuracy [21,36]. For a more in-depth discussion of the PML modes and the accuracy of the linear framework, the reader is referred to Ref. [11].

As a first evidence of the capabilities of the proposed framework, in Fig. 3 we plot the absorption and scattering cross sections of the graphene-strip scatterer (solid lines) at the vicinity of the third harmonic frequency after illumination with a TM-polarized, normally incident plane wave towards the $-\hat{\mathbf{y}}$ direction of the form $\mathbf{E}_{\mathrm{inc}} = E_0 \exp\{+jk_0y\}\hat{\mathbf{x}}$ with $E_0 = 1$ kV/cm here (harmonic time convention: $\exp\{+j\omega t\}$). The cross sections are calculated through the equations in Sec. S1.ii of the Supplemental Material [39] (see also [47]) by using the scattered field at 3ω, $\mathbf{E}_{\mathrm{sct}}^{(3\omega)}$, obtained through the QNM expansion utilizing the $a_m(3\omega)$ coefficients [Eq. (5)] as the weights of the sum. Note that each point on the graph corresponds to a different illumination frequency ω. A direct comparison with the respective results obtained using full-wave nonlinear simulations (blue circles) reveals the very high accuracy of the developed QNM framework. Due to the continuous wave (cw) nature of the excitation, the nonlinear full-wave simulation can be decomposed in two independent linear simulations. First, a linear scattering problem is solved at the fundamental frequency ω to retrieve $\mathbf{E}_{\mathrm{sct}}^{(\omega)}$. Then, the total field $\mathbf{E}_t^{(\omega)}$, i.e., the summation of the analytically known background field and the calculated scattered field, is used to calculate the nonlinear surface current $\mathbf{J}_{s,\mathrm{NL}}^{(3\omega)}$. This induced nonlinear surface current acts as a source for a second linear (radiation) problem at the third harmonic frequency 3ω. From the solution of the second linear problem, we can specify $\mathbf{E}_{\mathrm{sct}}^{(3\omega)}$ and, consequently, we are able to calculate the respective cross sections included in Fig. 3 with markers. The above process is repeated for each frequency point of Fig. 3, i.e., for N frequency points one has to solve $2N$ linear problems (N at ω and N at 3ω).
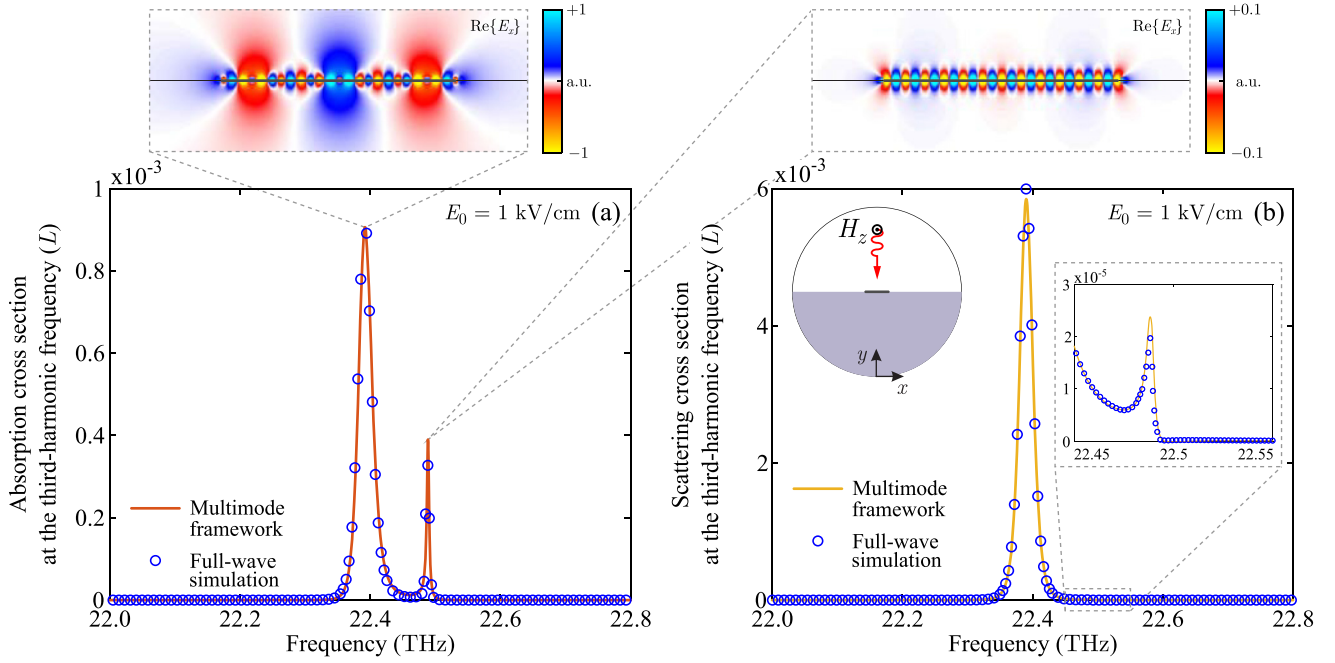
FIG. 3. Third harmonic generation with a graphene-strip scatterer on a semi-infinite glass substrate. Evaluation of the proposed nonlinear framework by comparing with full-wave simulations when $E_0 = 1$ kV/cm. (a) Absorption cross section at the third harmonic frequency in units of graphene strip length. Insets: E_x-field distribution as obtained from full-wave simulations at the two absorption peaks with the second lying exactly at the resonance frequency of the $m = 25$ QNM. (b) Scattering cross section at the third harmonic frequency in units of graphene strip length. Inset: zoomed-in plot around 22.49 THz where the second peak lies. Even weak spectral features are accurately resolved, testifying for the high accuracy of the proposed framework.

Interestingly, two distinct peaks appear in the absorption cross section [Fig. 3(a)]. As mentioned, due to graphene dispersion a higher-order resonance is not found at exactly $3\omega_{res,3}$. The simultaneous presence of resonances at exactly ω and 3ω is frequently termed double-resonant enhancement [40,48] and would correspond to conditions for optimum conversion efficiency. Here, this is not exactly the case, leading to two distinct peaks. The first peak emerges precisely at the third harmonic of the fundamental mode, i.e., at $3\omega_{res,3}/2\pi = 22.38$ THz. The second peak lies at the resonance frequency of the $m = 25$ order mode, i.e., at 22.49 THz. The fact that the enhanced conversion process at 22.49 THz is mediated by the $m = 25$ order mode is further corroborated by the distribution of the E_x component observed in the full-wave simulations (radiation by nonlinear current on graphene) [see inset in Fig. 3(a)]; it features exactly the same distribution as the pure $m = 25$ QNM extracted from the eigenmode analysis (cf. Fig. 2). On the contrary, since no QNM is found at exactly 22.38 THz, a hybrid field distribution is seen in the corresponding inset. The observation of the second peak is a consequence of the low quality factor of the fundamental ($m = 3$) mode. Given that $Q_{i,3} = 486.4$, the frequency $22.49/3 = 7.4967$ THz still lies under the Lorentzian of the fundamental mode and, thus, a non-negligible amount of light interacts with graphene and is up-converted. The second peak exhibits approximately half the amplitude of the first one due to the suboptimal coupling of the respective fundamental frequency (note that the field distributions in the insets have an order of magnitude difference). Finally, a secondary peak appears in the scattering cross section as well [inset of Fig. 3(b)], but with a much lower amplitude. This is attributed to the

corresponding resistive and radiative quality factors, which equal $Q_{res,25} = 5656.7$ and $Q_{rad,25} = 89\,766$, respectively, and to the fact that $\sigma_{abs} \propto r_Q/(1 + r_Q)^2$ while $\sigma_{sct} \propto 1/(1 + r_Q)^2$, with $r_Q = Q_{rad}/Q_{res}$ [4,49].

We stress that single-mode frameworks such as the classical form of the CMT [42,50–52], are not able to capture such a complex spectral behavior. On the contrary, the presented multimode framework captures the actual physical picture with multiple resonances being involved in the conversion process. Finally, note that if we want to shift the resonance positions and place a higher-order resonance exactly at the third harmonic of the fundamental frequency to enhance the conversion efficiency, we can do so by resorting to a finite-width scatterer and tuning the dimension along the z axis. This way, the underlying waveguide becomes of finite width introducing waveguide dispersion and providing an additional degree of freedom in shaping the total dispersion of the propagating GSP and, thus, the positions of the resonances [53].

B. Graphene-strip metasurface on a metal-backed glass substrate

For the second example, we switch to a periodic system, i.e., we expand the single graphene strip of the previous section into a metasurface, which is backed by a gold reflector to operate in reflection mode [Fig. 1(b)]. Metasurfaces and other periodic structures (gratings, photonic crystal membranes, frequency selective surfaces) are very important components in photonics. In order to be able to tackle the metasurface under study with the proposed framework, we will need to make several modifications; they are detailed in what follows.
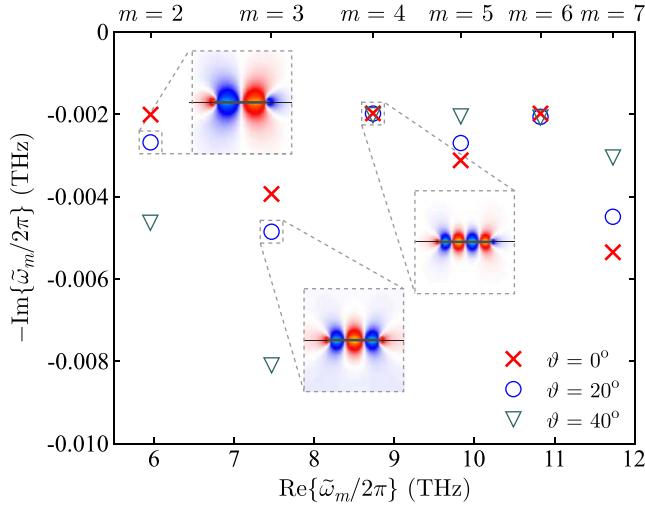
FIG. 4. Eigenmodes of the reflective graphene-strip metasurface: dependence of a few, low-order QNMs on the angle of incidence ϑ. The length of the graphene strip is $L = 5$ μm, while the pitch of the metasurface is $\Lambda = 10$ μm and the substrate height is $h = 19.5$ μm. For details on how the imaginary and real parts of the resonance frequencies vary, see the main text and Fig. S5 of the Supplemental Material [39]. Insets: E_x-field distribution of a few QNMs for $\vartheta = 20°$.

The length of the graphene strip remains the same, while the periodicity (lattice constant) is chosen as $\Lambda = 10$ μm (filling factor $f = 50\%$) and the height of the substrate as $h = 19.5$ μm. These two parameters were fine tuned to achieve perfect absorption for normal incidence with the $m = 3$ order QNM, eliminating any reflections and boosting conversion efficiency [53]. In terms of the corresponding quality factors, this is achieved when $Q_{\text{res}} = Q_{\text{rad}}$, frequently termed the critical coupling condition [54]. Furthermore, due to the small wavelength (large parallel wave vector) of propagating plasmons, the metasurface lattice constant is deeply subwavelength. It remains subwavelength even at the vicinity of the third harmonic frequency ($\lambda_{3\omega} \approx 13.4$ μm at 22.4 THz), meaning that only the zeroth diffraction order contributes to the reflection at normal incidence. The first diffraction order in reflection will start becoming propagating for $\vartheta \geqslant 20°$, as $\Lambda/\lambda_{3\omega} > 1/(\sin \vartheta + 1)$, but even for higher angles (e.g., 40°) considered in the simulations included here, we have found that it carries only a very small portion of the reflected power.

A small set of the supported QNMs around the fundamental frequency are shown in Fig. 4, considering different incidence angles ($\vartheta = 0°$, 20°, and 40°). They have been calculated assuming the phase advance conditions that would be imposed between the side-periodic boundary conditions [planes $x = -\Lambda/2$ and $+\Lambda/2$ in Fig. 1(b)] in excitation scenarios with obliquely incident plane waves. Note that the eigenvalue calculations are performed using a formulation involving the periodic envelope of the electric field [55,56] (Bloch-Floquet theorem); the information regarding the phase difference $|\mathbf{k}_F|\Lambda$ between periodic planes, which contains the unknown resonant frequency through $\mathbf{k}_F$, is included within the modified wave equation instead of an appropriate boundary condition [19]. See Appendix B for the emerging equation and a brief discussion.

Observing Fig. 4, the complex eigenfrequency of each mode changes depending on the angle of incidence. Both real and imaginary parts are affected (modifications to the real part are not practically observable due to scaling but are included in the Supplemental Material, Fig. S5 [39]). Interestingly, symmetric (m is odd) and antisymmetric (m is even) modes are affected differently (the symmetry of the modes is considered with respect to the $x = 0$ plane). Symmetric modes exhibit pronounced differences in the quality factor, which can either increase or decrease depending on the relation between the resonance wavelength and the height of the substrate. This is verified by considering the case of a transmissive metasurface without a backplane (infinite substrate); in this case, the quality factors obtained from the eigenvalue problem monotonically increase with increasing angle as radiation is suppressed (see the Supplemental Material, Sec. S2.ii [39]). Antisymmetric modes retain a practically constant quality factor, determined by the resistive component Q_{res}, which remains practically unchanged with ϑ due to the strong confinement of the field and the fact that Q_{rad} attains very high values. The only exception is the lowest-order, $m = 2$, mode which can become quite radiative as the incidence angle increases. A more comprehensive discussion regarding the dependence of the QNM eigenvalues on ϑ is included in the Supplemental Material, Sec. S2.i [39].

Subsequently, we use the obtained QNMs, as well as the accompanying spurious modes, to calculate the absorption and reflection at the third harmonic frequency. To do so, we have to modify the framework of Sec. II to correctly take into account the envelope formulation used to obtain the respective QNMs. To this end, we use the Bloch envelope $\tilde{\boldsymbol{\psi}}_m$ (lowercase), rather than the full field $\tilde{\boldsymbol{\Psi}}_m$, for obtaining the expansion coefficients [19]. Using $\tilde{\boldsymbol{\Psi}}_m(\mathbf{r}) = \tilde{\boldsymbol{\psi}}_m(\mathbf{r})\exp\{-j\mathbf{k}_{F,m}\cdot\mathbf{r}\} = \tilde{\boldsymbol{\psi}}_m(\mathbf{r})\exp\{-jk_{0,m}\boldsymbol{\eta}\cdot\mathbf{r}\}$ where $\mathbf{k}_{F,m} = k_{0,m}\boldsymbol{\eta}$ is the Bloch wave vector, the curl Maxwell's equations are transformed into $\hat{\mathcal{L}}\tilde{\boldsymbol{\psi}}_m = \tilde{\omega}_m\hat{\mathcal{M}}\tilde{\boldsymbol{\psi}}_m$ and the matrix operator

$$\hat{\mathcal{M}} = \begin{bmatrix} 1 & -(c_0\mu)^{-1}\boldsymbol{\eta}\times & 0 \\ (c_0\varepsilon)^{-1}\boldsymbol{\eta}\times & 1 & 0 \\ 0 & 0 & 1 \end{bmatrix} \quad (6)$$

is introduced to include the information of the incident wave direction through $\boldsymbol{\eta}$. For example, in a metasurface with periodicity along the x axis and under illumination with an incident angle ϑ, $\boldsymbol{\eta} = n_i \sin\vartheta\hat{\mathbf{x}}$ and n_i is the refractive index of the superstrate. Ultimately, the expansion coefficients take the form

$$a_m(\omega) = \frac{1}{\tilde{\omega}_m - \omega}\int_V \tilde{\mathbf{j}}_{-m}\cdot\mathbf{e}_{\text{inc}}dV, \quad (7)$$

and the normalization condition acquires an additional term related with $\boldsymbol{\eta}$, now becoming

$$\int_V \left[\tilde{\mathbf{e}}_{-m}\cdot\varepsilon\tilde{\mathbf{e}}_m - \tilde{\mathbf{h}}_{-m}\cdot\mu\tilde{\mathbf{h}}_m - \tilde{\mathbf{e}}_{-m}\cdot j\frac{\partial\bar{\bar{\sigma}}_s(\omega)}{\partial\omega}\tilde{\mathbf{e}}_m\delta_s \right.$$
$$\left. -\boldsymbol{\eta}\cdot\frac{1}{c_0}(\tilde{\mathbf{h}}_{-m}\times\tilde{\mathbf{e}}_m + \tilde{\mathbf{e}}_{-m}\times\tilde{\mathbf{h}}_m)\right]dV = 1. \quad (8)$$

Note that in Eqs. (7) and (8) the notation $\tilde{\boldsymbol{\psi}}_{-m}$ implies the use of the left eigenvectors [19,57]. In periodic systems comprising reciprocal materials they are found through

$\tilde{\mathbf{\Psi}}_{-m}(\mathbf{r}) = \tilde{\boldsymbol{\psi}}_{-m}(\mathbf{r}) \exp\{+jk_{0,m}\boldsymbol{\eta} \cdot \mathbf{r}\}$ while $\tilde{\boldsymbol{\psi}}_{-m}(\mathbf{r})$ can be obtained from $\tilde{\boldsymbol{\psi}}_{m}(\mathbf{r})$ through simple transformations [57]. In general, when nonreciprocal materials are involved or if structural asymmetries exist, left eigenvectors need to be calculated separately in order to construct the orthonormal basis that is required to obtain the expansion in QNMs [12,18,33,58]. We highlight again here that $\mathbf{E}_{\text{inc}}$ should be replaced with $\mathbf{E}_{b}$ in the presence of a substrate, as is the case considered here. Finally, the expansion coefficients at the third harmonic frequency are calculated through

$$a_m(3\omega) = \frac{-j}{\tilde{\omega}_m - 3\omega}$$
$$\times \int_V \left[\tilde{\mathbf{e}}_{-m} \cdot \mathbf{j}_{s,\text{NL}}^{(3\omega)}\delta_s - \boldsymbol{\eta} \cdot \frac{1}{c_0\varepsilon}\left(\tilde{\mathbf{h}}_{-m} \times \mathbf{j}_{s,\text{NL}}^{(3\omega)}\delta_s\right) \right] dV, \tag{9}$$

and involve an additional term compared to Eq. (5) which depends on $\boldsymbol{\eta}$. Note that the nonlinear surface current density at 3ω is defined as $\mathbf{j}_{s,\text{NL}}^{(3\omega)} = (\sigma_3/4)(\mathbf{e}_{t,\parallel}^{(\omega)} \cdot \mathbf{e}_{t,\parallel}^{(\omega)})\mathbf{e}_{t,\parallel}^{(\omega)}$, i.e., by using the spatial envelope $\mathbf{e}_t$ extracted from the total field $\mathbf{E}_t$ by removing the appropriate phase term $\exp\{-jk_0\boldsymbol{\eta} \cdot \mathbf{r}\}$.

Next, the structure is excited with a TM-polarized plane wave inside the xy plane ($\mathbf{H}_{\text{inc}} \equiv H_z\hat{\mathbf{z}}$) and the obtained results (reflected and absorbed power) are depicted in Fig. 5 for an input power (per period) of 100 W/m and an angle of incidence $\vartheta = 20°$. Note that this input power level corresponds to an electric field of $|E_{\text{inc}}^{(\omega)}| = 0.86$ kV/cm. This value is within current experimental capabilities. For example, in Ref. [59] an experiment was conducted at 0.3 THz with a peak electric field (pulsed operation) of $|E_{\text{inc}}^{(\omega)}| \sim 80$ kV/cm to reveal up to seventh harmonic generation in graphene. For the chosen input power level though, only THG is practically significant. Once again, excellent agreement with full-wave nonlinear simulations is attained. The main peak appears at 22.404 THz, exactly at $3\omega_{\text{res},3}$, while a second peak appears in this example as well, lying at $\omega_{\text{res},25}/2\pi = 22.489$ THz, which is the resonance frequency of the respective $m = 25$ QNM. In contrast to Fig. 3(a), the amplitude of this secondary peak is significantly suppressed since the fundamental frequency $22.489/3 = 7.496$ THz is not well accommodated under the respective Lorentzian, which is centered at $\omega_{\text{res},3}/2\pi = 7.468$ THz and possesses $Q_{i,3} = 769.3$. Nevertheless, the proposed framework succeeds in accurately capturing the amplitude and line shape of these weaker peaks as well (see insets of Fig. 5).

Finally, in Fig. 6 we keep the incident wave frequency constant at 7.468 THz, vary the power it carries, and examine the conversion efficiency from the fundamental to the third harmonic frequency [calculated as CE $= 10\ln(P_{\text{refl}}^{(3\omega)}/P_{\text{inc}})$]. The conversion efficiency increases with incident power as anticipated and exceeds -20 dB (1%); this efficient up-conversion is a result of the strong nonlinearity of graphene and the relatively high quality factor of the supported resonances. Clearly, the proposed framework and the nonlinear full-wave simulations are in excellent agreement over a wide range of P_{inc} values. We note again that the developed framework and the full-wave simulations are performed for the undepleted-pump scenario. This scenario is applicable under two main assumptions: First, the back-conversion from the third harmonic to
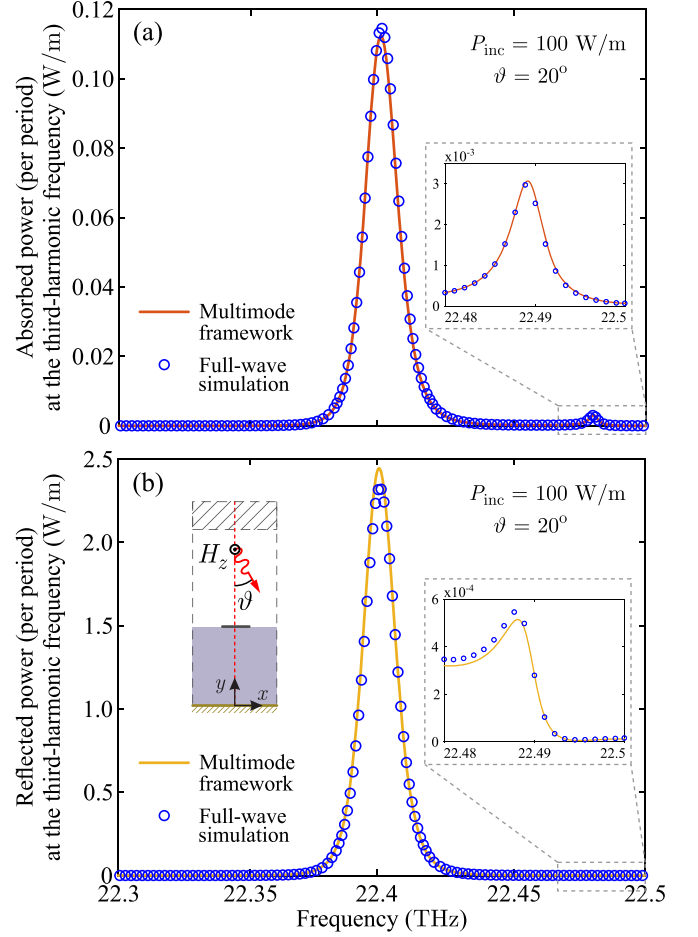

FIG. 5. Third harmonic generation with reflective graphene-strip metasurface. Comparison between the proposed multimode nonlinear framework and full-wave nonlinear simulations. (a) Absorption and (b) reflection at the third harmonic frequency. The incident field is a TM-polarized plane wave ($\mathbf{H}_{\text{inc}} \equiv H_z\hat{\mathbf{z}}$) at an incidence angle $\vartheta = 20°$. Insets: zoom-in around 22.49 THz where the second peak lies. The capabilities of the framework in reproducing the full-wave results are evident, even when weak and non-Lorentzian features are involved.

the fundamental frequency is negligible and, second, only a negligibly small portion of the pump power is depleted and converted to the third harmonic frequency. Both assumptions imply that the amplitude of the field at the fundamental frequency is only slightly changed by the conversion process. These assumptions are very reasonable for CEs up to -20 dB (1%) [42].

IV. CONCLUSION

We have proposed a modal formalism for studying third harmonic generation in non-Hermitian open resonant systems comprising 2D materials. It is constructed by expressing the scattered fields at the fundamental and third harmonic frequencies as expansions in a set of supported quasinormal modes. The infinitesimally thin and dispersive nature of 2D materials has been rigorously taken into account. A graphene-strip single scatterer and a periodic metasurface were selected
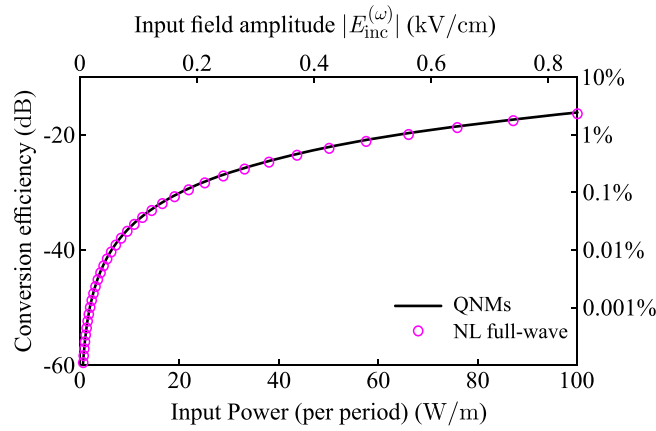
FIG. 6. Conversion efficiency of the graphene-strip metasurface versus incident power. The results obtained using the proposed QNM framework are in excellent agreement with nonlinear full-wave simulations over a wide range of P_{inc} values. The conversion efficiency can exceed -20 dB (1%) for realistic input intensities (see main text); this efficient up-conversion is a result of the strong nonlinearity of graphene and the high quality factor of the supported resonances.

as examples for demonstrating the framework capabilities. In both cases, excellent agreement with full-wave nonlinear simulations has been obtained. By providing insight into the full range of quasinormal modes supported by the structures, we were able to explain the spectral features of the nonlinear response arising due to the different resonant modes involved in the conversion process. In the reflective metasurface, the conversion efficiency can exceed -20 dB (1%) for realistic input intensities, highlighting the practical potential of graphene and 2D materials in general for nonlinear nanophotonics. The proposed framework combines computational efficiency along with the ability to acquire physical insight into the frequency generation process and provide guidelines for boosting the conversion by engineering the mode spectrum.

ACKNOWLEDGMENT

APPENDIX A: MULTIMODE QUASINORMAL-MODE FRAMEWORK FOR PHOTONIC SCATTERERS INCORPORATING BULK AND SHEET THIRD-ORDER NONLINEAR MATERIALS

In this Appendix, we present the complete derivation of our developed framework, which includes the general case of cavities with lossy, dispersive, and anisotropic materials. Furthermore, the resonant cavity can include both bulk and sheet-type materials. Although any combination is allowed, for the sake of the presentation we will assume a cavity consisting of a bulk material with a single Drude-Lorentz pole and a sheet material with a single Drude pole, i.e., described by the equations

$$\bar{\bar{\varepsilon}}(\omega) = \varepsilon_0 \bar{\bar{\varepsilon}}_\infty \left(1 - \frac{\omega_p^2}{\omega^2 - \omega_0^2 - j\omega\gamma_b} \right), \quad \text{(A1a)}$$

$$\bar{\bar{\sigma}}_s(\omega) = -j \frac{\bar{\bar{\sigma}}_0}{\omega - j\gamma_s}. \quad \text{(A1b)}$$

The parameters ω_p, ω_0, and γ_b are, respectively, the plasma frequency, resonance frequency, and damping factor of the bulk material. Additionally, $\bar{\bar{\varepsilon}}_\infty$ is the relative permittivity of the material at infinite frequency, which can be anisotropic. For the sheet material, γ_s is the damping factor and $\bar{\bar{\sigma}}_0/\gamma_s$ is the (anisotropic) conductivity at $\omega = 0$. Note that both $\bar{\bar{\varepsilon}}$ and $\bar{\bar{\sigma}}_s$ are spatially dependent, so that, e.g., $\bar{\bar{\sigma}}_s(\mathbf{r}) = \mathbf{0}$ outside the 2D material. For bulk materials without dispersion, as for example is commonly the case with the background permittivity ε_b of a photonic scatterer $\bar{\bar{\varepsilon}}(\mathbf{r}) = \varepsilon_0 \varepsilon_b \mathbf{I}_3$ ($\mathbf{I}_3$ is the 3×3 identity matrix).

To include both the bulk and sheet dispersive material in the framework, three auxiliary fields are needed, two for the Drude-Lorentz pole of the bulk material and one for the Drude pole of the 2D material [21,37]. More generally, a Drude-Lorentz pole requires always two auxiliary fields and a Drude pole only one. In our case, we define the auxiliary fields

$$\mathbf{P}_b = -\varepsilon_0 \bar{\bar{\varepsilon}}_\infty \frac{\omega_p^2}{\omega^2 - \omega_0^2 - j\omega\gamma_b} \mathbf{E}, \quad \text{(A2a)}$$

$$\mathbf{J}_b = j\omega \mathbf{P}_b, \quad \text{(A2b)}$$

$$\mathbf{J}_s = -\frac{\bar{\bar{\sigma}}_0}{\omega - j\gamma_s} \mathbf{E}\delta_s, \quad \text{(A2c)}$$

to accompany the electric $\mathbf{E}$ and magnetic $\mathbf{H}$ fields in the Maxwell's equations. Following the notation of the paper, the source-free curl Maxwell's equations are expressed in the compact notation $\hat{\mathcal{L}}\tilde{\boldsymbol{\Psi}}_m = \tilde{\omega}_m \tilde{\boldsymbol{\Psi}}_m$, where now $\tilde{\boldsymbol{\Psi}}_m = [\tilde{\mathbf{H}}_m \ \tilde{\mathbf{E}}_m \ \tilde{\mathbf{P}}_{b,m} \ \tilde{\mathbf{J}}_{b,m} \ \tilde{\mathbf{J}}_{s,m}]^T$ and

$$\hat{\mathcal{L}} = \begin{bmatrix} 0 & j\mu^{-1}\boldsymbol{\nabla}\times & 0 & 0 & 0 \\ -j(\varepsilon_0\bar{\bar{\varepsilon}}_\infty)^{-1}\boldsymbol{\nabla}\times & 0 & 0 & j(\varepsilon_0\bar{\bar{\varepsilon}}_\infty)^{-1} & -(\varepsilon_0\bar{\bar{\varepsilon}}_\infty)^{-1} \\ 0 & 0 & 0 & -j & 0 \\ 0 & -j(\varepsilon_0\bar{\bar{\varepsilon}}_\infty)\omega_p^2 & j\omega_0^2 & j\gamma_b & 0 \\ 0 & -\bar{\bar{\sigma}}_0\delta_s & 0 & 0 & j\gamma_s \end{bmatrix}. \quad \text{(A3)}$$

To find the expansion coefficients $a_m(\omega)$, one has to begin from the scattering formulation at the fundamental frequency. Then, the curl Maxwell's equations take the compact form $\hat{\mathcal{L}}\Psi_{\text{sct}}^{(\omega)} = \omega\Psi_{\text{sct}}^{(\omega)} + \mathbf{S}_{\text{inc}}^{(\omega)}$, where

$$\mathbf{S}_{\text{inc}}^{(\omega)} = \begin{bmatrix} \mathbf{0} \\ (1 - \varepsilon_b\bar{\bar{\varepsilon}}_\infty^{-1})\omega\mathbf{E}_{\text{inc}} \\ \mathbf{0} \\ j(\varepsilon_0\bar{\bar{\varepsilon}}_\infty)\omega_p^2\mathbf{E}_{\text{inc}} \\ \bar{\bar{\sigma}}_0\mathbf{E}_{\text{inc}}\delta_s \end{bmatrix}, \quad (A4)$$

showing that the incident field interacts both with the bulk and sheet material. Using Eq. (A4) and the Lorentz reciprocity theorem, it is easy to show that the expansion coefficients $a_m(\omega)$ are given by the general expression [21]

$$a_m(\omega) = \frac{1}{\tilde{\omega}_m - \omega}\frac{\int_V \tilde{\Psi}_m^T\hat{\mathbf{D}}\mathbf{S}_{\text{inc}}^{(\omega)}dV}{\int_V \tilde{\Psi}_m^T\hat{\mathbf{D}}\tilde{\Psi}_m dV}, \quad (A5)$$

with $\hat{\mathbf{D}} = \text{diag}(-\mu, \varepsilon_0\bar{\bar{\varepsilon}}_\infty, \omega_0^2(\omega_p^2\varepsilon_0\bar{\bar{\varepsilon}}_\infty)^{-1}, -(\omega_p^2\varepsilon_0\bar{\bar{\varepsilon}}_\infty)^{-1}, \bar{\bar{\sigma}}_0^{-1})$ being a diagonal matrix, suitable to apply the unconjugated Lorentz reciprocity theorem [37]. The denominator of Eq. (A5) is actually the QNM normalization factor, which can be cast in the expanded form

$$\int_V \left(\tilde{\mathbf{E}}_m \cdot \frac{\partial\{\omega\bar{\bar{\varepsilon}}(\omega)\}}{\partial\omega}\bigg|_{\omega=\tilde{\omega}_m}\tilde{\mathbf{E}}_m \right.$$
$$\left. - \tilde{\mathbf{H}}_m \cdot \mu\tilde{\mathbf{H}}_m - \tilde{\mathbf{E}}_m \cdot j\frac{\partial\bar{\bar{\sigma}}(\omega)}{\partial\omega}\bigg|_{\omega=\tilde{\omega}_m}\tilde{\mathbf{E}}_m\delta_s \right)dV = 1, \quad (A6)$$

and includes the dispersive properties of both bulk and sheet-type materials through the spectral derivatives $\partial\{\omega\bar{\bar{\varepsilon}}(\omega)\}/\partial\omega$ and $\partial\bar{\bar{\sigma}}(\omega)/\partial\omega$, respectively. Henceforth, we assume that all the QNMs are appropriately normalized according to Eq. (A6). With this in mind, the expansion coefficients of Eq. (A5) take the more useful form

$$a_m(\omega) = \frac{1}{\tilde{\omega}_m - \omega}\int_V \left[\tilde{\mathbf{E}}_m \cdot \omega\varepsilon_0(\bar{\bar{\varepsilon}}_\infty - \varepsilon_b)\mathbf{E}_{\text{inc}} \right.$$
$$+ \tilde{\mathbf{E}}_m \cdot \tilde{\omega}_m\varepsilon_0(\bar{\bar{\varepsilon}}_r(\tilde{\omega}_m) - \bar{\bar{\varepsilon}}_\infty)\mathbf{E}_{\text{inc}}$$
$$\left. - \tilde{\mathbf{E}}_m \cdot \frac{\bar{\bar{\sigma}}_0}{\tilde{\omega}_m - j\gamma_s}\mathbf{E}_{\text{inc}}\delta_s \right]dV. \quad (A7)$$

It is easy to see how Eq. (A7) expands the framework of Ref. [21] since it now includes the contribution of both bulk and sheet-type dispersive materials. One can also see that Eq. (2) is a simplified version of Eq. (A7). Note that in Eq. (A7), we have used the notation $\bar{\bar{\varepsilon}}_r(\tilde{\omega}_m) = \bar{\bar{\varepsilon}}(\tilde{\omega}_m)/\varepsilon_0$. Furthermore, we shall highlight again that in the presence of a reflected wave, the incident field $\mathbf{E}_{\text{inc}}$ should be replaced with the background field $\mathbf{E}_b$ throughout the calculations.

At the third harmonic frequency, a similar approach can be followed to retrieve the respective coefficients. We allow for the general case where both the bulk and sheet-type materials exhibit nonlinearities of the same form, induced using the nonlinear counterpart of the auxiliary fields $\mathbf{P}_b$ and $\mathbf{J}_s$,

respectively, i.e.,

$$\mathbf{P}_{b,\text{NL}}^{(3\omega)} = (\chi_3/4)\big(\mathbf{E}_t^{(\omega)} \cdot \mathbf{E}_t^{(\omega)}\big)\mathbf{E}_t^{(\omega)}, \quad (A8a)$$

$$\mathbf{J}_{s,\text{NL}}^{(3\omega)} = (\sigma_3/4)\big(\mathbf{E}_{t,\|}^{(\omega)} \cdot \mathbf{E}_{t,\|}^{(\omega)}\big)\mathbf{E}_{t,\|}^{(\omega)}, \quad (A8b)$$

with the subscript "t" denoting the total field as the sum of the incident, reflected from the background and scattered fields. The use of these auxiliary fields which actually coincide with the respective nonlinear polarization and surface current quantities is a natural selection when electronic nonlinearities are described [42]. The scattered field formulation at 3ω acquires the compact form $\hat{\mathcal{L}}\Psi_{\text{sct}}^{(3\omega)} = 3\omega\Psi_{\text{sct}}^{(3\omega)} + \mathbf{S}_{\text{inc}}^{(3\omega)}$, where the source term is given by

$$\mathbf{S}_{\text{inc}}^{(3\omega)} = \begin{bmatrix} \mathbf{0} \\ -j(\varepsilon_0\bar{\bar{\varepsilon}}_\infty)^{-1}[j(3\omega)\mathbf{P}_{b,\text{NL}} + \mathbf{J}_{s,\text{NL}}\delta_s] \\ \mathbf{0} \\ \mathbf{0} \\ \mathbf{0} \end{bmatrix}, \quad (A9)$$

i.e., it only contributes as a right-hand-side term in the Ampère-Maxwell equation. Using $\mathbf{S}_{\text{inc}}^{(3\omega)}$ in Eq. (A5), the expansion coefficients for the third harmonic frequency can be calculated through

$$a_m(3\omega) = \frac{1}{\tilde{\omega}_m - 3\omega}$$
$$\times \int_V \big(3\omega\tilde{\mathbf{E}}_m \cdot \mathbf{P}_{b,\text{NL}}^{(3\omega)} - j\tilde{\mathbf{E}}_m \cdot \mathbf{J}_{s,\text{NL}}^{(3\omega)}\delta_s\big)dV. \quad (A10)$$

Equation (A10) is a generalized version of Eq. (5) to include the more general case of cavities with both bulk and sheet-type third-order nonlinear materials. This equation is presented in the context of *multimode non-Hermitian* systems. In our recent works, the simpler case of *single-mode quasi-Hermitian* systems has been addressed [38,42].

As a final remark, we note that materials with multiple Drude-Lorentz poles can be introduced in the formulation simply by using an appropriate number of auxiliary fields to represent the respective poles. Examples of such a scenario are noble metals with interband transitions above the plasma frequency or dielectric materials described by a Sellmeier equation of the general form

$$n^2(\lambda) = n_0^2 + \sum_{k=1}^{3}\frac{B_k\lambda^2}{\lambda^2 - C_k^2}. \quad (A11)$$

Equation (A11) introduces three poles in the system, thus six auxiliary fields are needed for its correct representation. It is more convenient to express Eq. (A11) as a function of the angular frequency instead of the wavelength and to use the permittivity instead of the refractive index, i.e.,

$$\varepsilon(\omega) = \varepsilon_0\varepsilon_\infty\left(1 - \sum_{k=1}^{3}\frac{\omega_{p,k}^2}{\omega^2 - \omega_{0,k}^2}\right), \quad (A12)$$

where $\omega_{p,k} = 2\pi c_0\sqrt{B_k/(n_0C_k)^2}$ and $\omega_{0,k} = 2\pi c_0\sqrt{1/C_k^2}$ are the plasma frequency and the resonance frequency of each pole while $\varepsilon_\infty \equiv n_0^2$; typically, no losses are included in the Sellmeier equation since it is used to describe dielectric materials and thus $\gamma_{p,k} = 0$. The expansion of the framework to

resonant structures consisting of multiple bulk and/or sheet materials with multiple poles each is trivial following the above description.

APPENDIX B: e-FIELD ENVELOPE FORMULATION FOR PERIODIC STRUCTURES

In this second Appendix, we will present the periodic envelope formulation (**e**-field envelope formulation), which is used in order to correctly calculate the QNMs of any resonant metasurface under oblique incidence. This stems from the implementation of the Bloch-Floquet periodic condition where the periodicity vector $\mathbf{k}_F$ needs to be specified. However, $|\mathbf{k}_F|$ depends on the unknown resonant frequency. This complication can be lifted by expressing the full field $\mathbf{E}(\mathbf{r})$ using the Bloch-Floquet theorem, which states that

$$\mathbf{E}(\mathbf{r}) = \mathbf{e}(\mathbf{r}) \exp\{-j\mathbf{k}_F \cdot \mathbf{r}\} = \mathbf{e}(\mathbf{r}) \exp\{-jk_0 \boldsymbol{\eta} \cdot \mathbf{r}\}, \quad \text{(B1)}$$

where $k_0 = \omega/c$ is now scalar and the vector $\boldsymbol{\eta}$ carries the information of the incident wave direction and the electromagnetic properties of the semi-infinite space on the side of incidence; for instance, in a metasurface with periodicity along the x axis and under illumination with an incident angle ϑ, $\boldsymbol{\eta} = n_i \sin\vartheta \hat{\mathbf{x}}$. This notation allows the inclusion of the term ω/c within the modified wave equation and not as a surface contribution in the respective periodic condition. More specifically, we start from the source-free Helmholtz equation for the full field in an eigenvector notation

$$\nabla \times \mu^{-1} \nabla \times \tilde{\mathbf{E}}_m - \tilde{\omega}_m^2 \varepsilon \tilde{\mathbf{E}}_m - \tilde{\omega}_m \tilde{\mathbf{J}}_m = 0. \quad \text{(B2)}$$

We then introduce the Bloch-Floquet theorem through Eq. (B1) (and a respective equation for the current term $\mathbf{J} = \mathbf{j} \exp\{-jk_0\boldsymbol{\eta} \cdot \mathbf{r}\}$) and after some trivial algebra arrive at the respective equation for the envelope $\mathbf{e}(\mathbf{r})$ [55,56]

$$\begin{aligned} &\nabla \times \mu^{-1}\nabla \times \tilde{\mathbf{e}}_m \\ &- j\frac{\tilde{\omega}_m}{c_0}\nabla \times \mu^{-1}(\boldsymbol{\eta} \times \tilde{\mathbf{e}}_m) - j\frac{\tilde{\omega}_m}{c_0}\boldsymbol{\eta} \times \mu^{-1}\nabla \times \tilde{\mathbf{e}}_m \\ &- \frac{\tilde{\omega}_m^2}{c_0^2}\boldsymbol{\eta} \times \mu^{-1}\boldsymbol{\eta} \times \tilde{\mathbf{e}}_m - \tilde{\omega}_m^2\varepsilon\tilde{\mathbf{e}}_m - \tilde{\omega}_m\tilde{\mathbf{j}}_m = 0. \end{aligned} \quad \text{(B3)}$$

Equation (B3) is the modified wave equation for the envelope; all the required information about the direction of the incident wave and the periodicity is included within the equation through $\boldsymbol{\eta}$. Since the envelope is a spatially periodic quantity and thus continuous in the boundaries of the unit cell, no Bloch-Floquet periodic boundary conditions are required; rather, a simple continuity condition is applied. In the context of this work, Eq. (B3) should be accompanied by the auxiliary field equation for graphene, which emerges from, e.g., Eq. (A2c) under the transformation introduced with Eq. (B1),

$$(\tilde{\omega}_m - j\gamma)\tilde{\mathbf{j}}_m + \bar{\bar{\sigma}}_0\tilde{\mathbf{e}}_m\delta_s = 0. \quad \text{(B4)}$$

Equations (B3) and (B4) can be solved by the generic FEM eigensolver of COMSOL to get the correct QNMs for the considered system.

---

[1] M. Taghinejad and W. Cai, All-optical control of light in micro- and nanophotonics, ACS Photonics **6**, 1082 (2019).

[2] G. Li, S. Zhang, and T. Zentgraf, Nonlinear photonic metasurfaces, Nat. Rev. Mater. **2**, 17010 (2017).

[3] R. W. Boyd, *Nonlinear Optics*, 3rd ed. (Academic, New York, 2008).

[4] T. Christopoulos, O. Tsilipakos, G. Sinatkas, and E. E. Kriezis, On the calculation of the quality factor in contemporary photonic resonant structures, Opt. Express **27**, 14505 (2019).

[5] C. Sauvan, J. P. Hugonin, I. S. Maksymov, and P. Lalanne, Theory of the Spontaneous Optical Emission of Nanosize Photonic and Plasmon Resonators, Phys. Rev. Lett. **110**, 237401 (2013).

[6] A. Autere, H. Jussila, Y. Dai, Y. Wang, H. Lipsanen, and Z. Sun, Nonlinear optics with 2d layered materials, Adv. Mater. **30**, 1705963 (2018).

[7] B. Guo, Q. lan Xiao, S. hao Wang, and H. Zhang, 2d layered materials: Synthesis, nonlinear optical properties, and device applications, Laser Photon. Rev. **13**, 1800327 (2019).

[8] K. F. Mak and J. Shan, Photonics and optoelectronics of 2d semiconductor transition metal dichalcogenides, Nat. Photonics **10**, 216 (2016).

[9] G. Sinatkas, T. Christopoulos, O. Tsilipakos, and E. E. Kriezis, Electro-optic modulation in integrated photonics, J. Appl. Phys. **130**, 010901 (2021).

[10] N. Matthaiakakis, S. Droulias, and G. Kakarantzas, Dynamic control of light chirality with nanostructured monolayer black phosphorus for broadband terahertz applications, Adv. Opt. Mater. **10**, 2102273 (2022).

[11] P. Lalanne, W. Yan, K. Vynck, C. Sauvan, and J.-P. Hugonin, Light interaction with photonic and plasmonic resonances, Laser Photon. Rev. **12**, 1700113 (2018).

[12] P. T. Kristensen, K. Herrmann, F. Intravaia, and K. Busch, Modeling electromagnetic resonators using quasinormal modes, Adv. Opt. Photon. **12**, 612 (2020).

[13] T. Wu, M. Gurioli, and P. Lalanne, Nanoscale light confinement: The q's and v's, ACS Photonics **8**, 1522 (2021).

[14] C. Sauvan, T. Wu, R. Zarouf, E. A. Muljarov, and P. Lalanne, Normalization, orthogonality, and completeness of quasinormal modes of open systems: the case of electromagnetism [invited], Opt. Express **30**, 6846 (2022).

[15] S. Both and T. Weiss, Resonant states and their role in nanophotonics, Semicond. Sci. Technol. **37**, 013002 (2022).

[16] M. B. Doost, W. Langbein, and E. A. Muljarov, Resonant-state expansion applied to three-dimensional open optical systems, Phys. Rev. A **90**, 013834 (2014).

[17] E. A. Muljarov and W. Langbein, Exact mode volume and purcell factor of open optical systems, Phys. Rev. B **94**, 235438 (2016).

[18] T. Weiss, M. Schäferling, H. Giessen, N. A. Gippius, S. G. Tikhodeev, W. Langbein, and E. A. Muljarov, Analytical normalization of resonant states in photonic crystal slabs and periodic arrays of nanoantennas at oblique incidence, Phys. Rev. B **96**, 045129 (2017).

[19] A. Gras, W. Yan, and P. Lalanne, Quasinormal-mode analysis of grating spectra at fixed incidence angles, Opt. Lett. **44**, 3494 (2019).

[20] E. A. Muljarov and W. Langbein, Resonant-state expansion of dispersive open optical systems: Creating gold from sand, Phys. Rev. B **93**, 075417 (2016).

[21] W. Yan, R. Faggiani, and P. Lalanne, Rigorous modal analysis of plasmonic nanoresonators, Phys. Rev. B **97**, 205422 (2018).

[22] N. Kongsuwan, A. Demetriadou, M. Horton, R. Chikkaraddy, J. J. Baumberg, and O. Hess, Plasmonic nanocavity modes: From near-field to far-field radiation, ACS Photonics **7**, 463 (2020).

[23] A. G. Primo, N. C. Carvalho, C. M. Kersul, N. C. Frateschi, G. S. Wiederhecker, and T. P. Mayer Alegre, Quasinormal-Mode Perturbation Theory for Dissipative and Dispersive Optomechanics, Phys. Rev. Lett. **125**, 233601 (2020).

[24] Q. Zhou, P. Zhang, and X.-W. Chen, Quasinormal mode theory for nanoscale electromagnetism informed by quantum surface response, Phys. Rev. B **105**, 125419 (2022).

[25] J. Ren, S. Franke, and S. Hughes, Connecting classical and quantum mode theories for coupled lossy cavity resonators using quasinormal modes, ACS Photonics **9**, 138 (2022).

[26] J. Ren, S. Franke, and S. Hughes, Quasinormal mode theory of chiral power flow from linearly polarized dipole emitters coupled to index-modulated microring resonators close to an exceptional point, ACS Photonics **9**, 1315 (2022).

[27] S. V. Lobanov, W. Langbein, and E. A. Muljarov, Resonant-state expansion applied to three-dimensional open optical systems: Complete set of static modes, Phys. Rev. A **100**, 063811 (2019).

[28] C. Sauvan, Quasinormal modes expansions for nanoresonators made of absorbing dielectric materials: Study of the role of static modes, Opt. Express **29**, 8268 (2021).

[29] J. Yang, H. Giessen, and P. Lalanne, Simple analytical expression for the peak-frequency shifts of plasmonic resonances for sensing, Nano Lett. **15**, 3439 (2015).

[30] S. Both and T. Weiss, First-order perturbation theory for changes in the surrounding of open optical resonators, Opt. Lett. **44**, 5917 (2019).

[31] W. Yan, P. Lalanne, and M. Qiu, Shape Deformation of Nanoresonator: A Quasinormal-Mode Perturbation Theory, Phys. Rev. Lett. **125**, 013901 (2020).

[32] T. Christopoulos, O. Tsilipakos, and E. E. Kriezis, Perturbation theory for kerr nonlinear leaky cavities, Opt. Lett. **45**, 6442 (2020).

[33] H. Zhang and O. D. Miller, Quasinormal coupled mode theory, arXiv:2010.08650.

[34] M. Benzaouia, J. D. Joannopoulos, S. G. Johnson, and A. Karalis, Quasi-normal mode theory of the scattering matrix, enforcing fundamental constraints for truncated expansions, Phys. Rev. Res. **3**, 033228 (2021).

[35] M. Zhou, D. Liu, S. W. Belling, H. Cheng, M. A. Kats, S. Fan, M. L. Povinelli, and Z. Yu, Inverse design of metasurfaces based on coupled-mode theory and adjoint optimization, ACS Photonics **8**, 2265 (2021).

[36] C. Gigli, T. Wu, G. Marino, A. Borne, G. Leo, and P. Lalanne, Quasinormal-mode non-hermitian modeling and design in nonlinear nano-optics, ACS Photonics **7**, 1197 (2020).

[37] A. Raman and S. Fan, Perturbation theory for plasmonic modulation and sensing, Phys. Rev. B **83**, 205131 (2011).

[38] T. Christopoulos, O. Tsilipakos, N. Grivas, and E. E. Kriezis, Coupled-mode-theory framework for nonlinear resonators comprising graphene, Phys. Rev. E **94**, 062219 (2016).

[39] See Supplemental Material at http://link.aps.org/supplemental/10.1103/PhysRevB.107.035413 for additional simulation results.

[40] A. Rodriguez, M. Soljačić, J. D. Joannopoulos, and S. G. Johnson, $\chi(2)$ and $\chi(3)$ harmonic generation at a critical power in inhomogeneous doubly resonant cavities, Opt. Express **15**, 7303 (2007).

[41] H. Hashemi, A. W. Rodriguez, J. D. Joannopoulos, M. Soljačić, and S. G. Johnson, Nonlinear harmonic generation and devices in doubly resonant Kerr cavities, Phys. Rev. A **79**, 013812 (2009).

[42] T. Christopoulos, O. Tsilipakos, G. Sinatkas, and E. E. Kriezis, Degenerate four-wave mixing in nonlinear resonators comprising two-dimensional materials: A coupled-mode theory approach, Phys. Rev. B **98**, 235421 (2018).

[43] Y. V. Bludov, A. Ferreira, N. M. R. Peres, and M. I. Vasilevskiy, A primer on surface plasmon-polaritons in graphene, Int. J. Mod. Phys. B **27**, 1341001 (2013).

[44] G. W. Hanson, Dyadic Green's functions and guided surface waves for a surface conductivity model of graphene, J. Appl. Phys. **103**, 064302 (2008).

[45] J. L. Cheng, N. Vermeulen, and J. E. Sipe, Third order optical nonlinearity of graphene, New J. Phys. **16**, 053014 (2014).

[46] A. Y. Nikitin, T. Low, and L. Martin-Moreno, Anomalous reflection phase of graphene plasmons and its influence on resonators, Phys. Rev. B **90**, 041407(R) (2014).

[47] Q. Bai, M. Perrin, C. Sauvan, J.-P. Hugonin, and P. Lalanne, Efficient and intuitive method for the analysis of light scattering by a resonant nanostructure, Opt. Express **21**, 27371 (2013).

[48] J. W. You, J. You, M. Weismann, and N. C. Panoiu, Double-resonant enhancement of third-harmonic generation in graphene nanostructures, Philos. Trans. R. Soc. A **375**, 20160313 (2017).

[49] D. Conteduca, G. S. Arruda, I. Barth, Y. Wang, T. F. Krauss, and E. R. Martins, Beyond q: The importance of the resonance amplitude for photonic sensors, ACS Photonics **9**, 1757 (2022).

[50] S. Fan, W. Suh, and J. D. Joannopoulos, Temporal coupled-mode theory for the fano resonance in optical resonators, J. Opt. Soc. Am. A **20**, 569 (2003).

[51] R. E. Hamam, A. Karalis, J. D. Joannopoulos, and M. Soljačić, Coupled-mode theory for general free-space resonant scattering of waves, Phys. Rev. A **75**, 053801 (2007).

[52] O. Tsilipakos, T. Christopoulos, and E. E. Kriezis, Long-range hybrid plasmonic disk resonators for mW bistability and self-pulsation, J. Lightwave Technol. **34**, 1333 (2016).

[53] A. Theodosi, O. Tsilipakos, C. M. Soukoulis, E. N. Economou, and M. Kafesaki, 2d-patterned graphene metasurfaces for efficient third harmonic generation at THz frequencies, Opt. Express **30**, 460 (2022).

[54] O. Tsilipakos, L. Maiolo, F. Maita, R. Beccherelli, M. Kafesaki, E. E. Kriezis, T. V. Yioultsis, and D. C. Zografopoulos, Experimental demonstration of ultrathin broken-symmetry meta-

surfaces with controllably sharp resonant response, Appl. Phys. Lett. **119**, 231601 (2021).

[55] M. Davanco, Y. Urzhumov, and G. Shvets, The complex bloch bands of a 2d plasmonic crystal displaying isotropic negative refraction, Opt. Express **15**, 9681 (2007).

[56] C. Fietz, Y. Urzhumov, and G. Shvets, Complex k band diagrams of 3d metamaterial/photonic crystals, Opt. Express **19**, 19027 (2011).

[57] P. Lalanne, W. Yan, A. Gras, C. Sauvan, J.-P. Hugonin, M. Besbes, G. Demésy, M. D. Truong, B. Gralak, F. Zolla, A. Nicolet, F. Binkowski, L. Zschiedrich, S. Burger, J. Zimmerling, R. Remis, P. Urbach, H. T. Liu, and T. Weiss, Quasinormal mode solvers for resonators with dispersive materials, J. Opt. Soc. Am. A **36**, 686 (2019).

[58] T. Weiss and E. A. Muljarov, How to calculate the pole expansion of the optical scattering matrix from the resonant states, Phys. Rev. B **98**, 085433 (2018).

[59] H. A. Hafez, S. Kovalev, K.-J. Tielrooij, M. Bonn, M. Gensch, and D. Turchinovich, Terahertz nonlinear optics of graphene: From saturable absorption to high-harmonics generation, Adv. Opt. Mater. **8**, 1900771 (2019).